The Role of Core-collapse Physics in the Observability of Black Hole Neutron Star Mergers as Multimessenger Sources

Jaime Román-Garza[1] , Simone S. Bavera[1] , Tassos Fragos[1] , Emmanouil Zapartas[1] , Devina Misra[1] , Jeff Andrews[2] , Scotty Coughlin[2] , Aaron Dotter[2] , Konstantinos Kovlakas[3,4] , Juan Gabriel Serra[2], Ying Qin[2,5] , Kyle A. Rocha[2] , and Nam Hai Tran[6]

[1] Departement d'Astronomie, Université de Genève, Chemin Pegasi 51, CH-1290 Versoix, Switzerland; jaime.roman@etu.unige.ch
[2] Center for Interdisciplinary Exploration and Research in Astrophysics (CIERA) and Department of Physics and Astronomy, Northwestern University, 1800 Sherman Avenue, Evanston, IL 60201, USA
[3] Physics Department, University of Crete, GR 71003 Heraklion, Greece
[4] Institute of Astrophysics, Foundation for Research and Technology-Hellas, GR 71110 Heraklion, Greece
[5] Department of Physics, Anhui Normal University, Wuhu, Anhui 241000, People's Republic of China
[6] DARK, Niels Bohr Institute, University of Copenhagen, Jagtvej 128, DK-2200 Copenhagen, Denmark

Abstract

Recent 1D core-collapse simulations indicate a nonmonotonicity of the explodability of massive stars with respect to their precollapse core masses, which is in contrast to commonly used prescriptions. In this work, we explore the implications of these results on the formation of coalescing black hole (BH)–neutron star (NS) binaries. Furthermore, we investigate the effects of natal kicks and the NS's radius on the synthesis of such systems and potential electromagnetic counterparts (EMCs) linked to them. Models based on 1D core-collapse simulations result in a BH–NS merger detection rate ($\sim 2.3\,\mathrm{yr}^{-1}$), 5–10 times larger than the predictions of "standard" prescriptions. This is primarily due to the formation of low-mass BHs via direct collapse, and hence no natal kicks, favored by the 1D simulations. The fraction of observed systems that will produce an EMC, with the supernova engine from 1D simulations, ranges from 2% to 25%, depending on the NS equation of state. Notably, in most merging systems with EMCs, the NS is the first-born compact object, as long as the NS's radius is $\lesssim 12$ km. Furthermore, models with negligible kicks for low-mass BHs increase the detection rate of GW190426_152155-like events to $\sim 0.6\,\mathrm{yr}^{-1}$, with an associated probability of EMC $\leqslant 10\%$ for all supernova engines. Finally, models based on 1D core-collapse simulations predict a ratio of BH–NSs to binary BHs' merger rate density that is at least twice as high as other prescriptions, but at the same time overpredicting the measured local merger density rate of binary black holes.

Unified Astronomy Thesaurus concepts: Gravitational waves (678); Black holes (162); Neutron stars (1108); Binary stars (154)

1. Introduction

The recently released catalog of the LIGO Scientific and Virgo Collaboration (LVC), GWTC-2, includes for the first time an event, GW190426_152155, classified as a black hole (BH)–neutron star (NS) merger (Abbott et al. 2020a). In addition, GW190814, an extreme mass ratio merger event, has an estimated mass of $2.59^{+0.08}_{-0.09}$ for the lower-mass compact object, making it unclear whether it is a binary BH (BBH) or a BH–NS (BHNS) merger (Abbott et al. 2020b; Han et al. 2020). Due to the relatively low significance of GW190426_152155 and the unclear nature of GW190814, no BHNS merger rate density was estimated based on GWTC-2 (Abbott et al. 2020c), with the older estimates from GWTC-1 setting only an upper limit of $< 610\,\mathrm{Gpc}^3\,\mathrm{yr}^{-1}$ (Abbott et al. 2019). Nevertheless, taking into account that the first half of the LVC's third observing run (O3a) included 177.3 days of data suitable for coincident analysis and assuming one or two detections, one can estimate a detection rate of ~ 2–$4\,\mathrm{yr}^{-1}$.

The first detection of a binary NS merger was accompanied by an electromagnetic counterpart (EMC), which was observed in the whole electromagnetic spectrum as a kilonova and a short gamma-ray burst (Abbott et al. 2017a, 2017b). The merger of a BH with an NS is also expected to be accompanied by a similar EMC, if the tidal disruption radius of the NS is outside the innermost stable circular orbit (ISCO) of the BH.

The maximum mass of a nonspinning BH for this to happen, assuming a $1.4\,M_\odot$ NS, is $\sim 3.5\,M_\odot$, with the exact value depending on the adopted NS equation of state (e.g., Capano et al. 2020). If, however, the BH is spinning, then the ISCO moves closer to the BH and the corresponding BH mass limit becomes as high as $\sim 20\,M_\odot$ for a maximally spinning BH (see Foucart et al. 2018), vastly increasing the probability of an EMC.

If we assume efficient angular momentum transport in the interior of stars, the first-born compact object in an isolated binary is expected to be formed with negligible spin (Fragos & McClintock 2015; Qin et al. 2018). This is because as the progenitor star expands to become a supergiant, most of its angular momentum is transported to its outer layers (Spruit 2002; Fuller et al. 2019), which are then removed via winds and Roche lobe overflow. On the other hand, the immediate progenitor of the second-born compact object, in the isolated binary formation channels, is a stripped helium (He) star in a close orbit with its first-born compact-object companion. There, the He star has a chance to be spun up via tides and thus to give rise to a compact object with a significant spin (e.g., Van den Heuvel & Yoon 2007; Qin et al. 2018; Bavera et al. 2020, 2021). Hence, the only way to have a highly spinning BH in a BHNS system, from the isolated binary formation channel given the previous assumptions, is to

have the NS be the first-born compact object, which will then tidally spin up the BH's progenitor star. If one relaxes the assumption of efficient angular momentum transport (see, e.g., Belczynski et al. 2020) and/or considers other formation channels that include dynamical interaction in dense stellar systems (e.g., Arca Sedda 2020; Rastello et al. 2020), then other formation pathways open up. However, the currently observed BBH population already favors negligible natal BH spin, even when one considers multiple formation channels (Zevin et al. 2021).

Coalescing BHNSs formed via isolated binary evolution are thought to be sufficiently abundant, with theoretical estimates of their merger rate density covering the whole range of 0.1–$1000\,\mathrm{Gpc}^3\,\mathrm{yr}^{-1}$ (Giacobbo & Mapelli 2018; Belczynski et al. 2020; Drozda et al. 2020). This large range of predicted merger rate densities is due to a number of uncertain model parameters, such as supernova (SN) kicks (e.g., Sipior & Sigurdsson 2002). Among the coalescing BHNSs, however, the ones in which the NS is the first-born compact object should be rare for two main reasons: (i) the initially more massive primary star is typically the progenitor of the BH that tends to form first, and (ii) even if binary interactions reverse the pre-core-collapse mass of the primary and secondary (Pols 1994; Belczynski & Taam 2008), kicks imparted on newly born NSs (Hobbs et al. 2005), which are expected to be higher than those on BHs, tend to disrupt the binary when the system is in a wide orbit, as is typically the case when the first compact object is formed.

The details of the general statements above depend crucially on the physics of core-collapse and compact-object formation. The vast majority of binary population synthesis (BPS) studies use the "rapid" and "delayed" mechanisms (Fryer et al. 2012) to prescribe the fate of massive stars. Both of them are parametric descriptions of the convection-enhanced SN engine driven by neutrino losses (see Herant et al. 1994). In contrast to the "delayed" one, the "rapid" prescription predicts a mass gap between BHs and NSs owing to stronger convection that allows instabilities to grow rapidly and produces more energetic SN explosions. Furthermore, both mechanisms predict a unique boundary in the core mass of the pre-core-collapse star that leads to the formation of a BH or an NS, above or below that boundary, respectively.

Recent 1D core-collapse simulations, on the other hand, show that there is no unique boundary in the core mass of the pre-core-collapse star that transitions between the formation of NSs and BHs. Instead, these studies find successive islands of successful and failed explosions leading to the formation of NSs and BHs via direct collapse, respectively (e.g., O'Connor & Ott 2011; Ugliano et al. 2012; Pejcha & Thompson 2015; Sukhbold et al. 2016; Ertl et al. 2020; Patton & Sukhbold 2020; Schneider et al. 2021). This is the result of the nonmonotonic behavior between the central carbon-burning phase and the final core properties, linked to the convective episodes developed during the burning phase (e.g., Sukhbold et al. 2018; Sukhbold & Woosley 2014). Another significant difference between these more recent calculations and the "rapid" and "delayed" prescriptions is in the formation of BHs via successful explosions and significant fallback. Whereas in the "rapid" and "delayed" prescriptions there is a wide range of pre-core-collapse core masses that lead to the formation of BHs via accretion of fallback mass from a successful explosion, 1D simulations find that these cases are very rare and virtually all

BHs are formed via direct collapse. The latter becomes important in the context of BPS studies, where the natal kicks imparted on BHs are most often rescaled to the fraction of fallback mass, while BHs formed via direct collapse receive no kick for this given prescription (e.g., Belczynski et al. 2008).

Astrometric observations of BH X-ray binaries provide indications that at least some BHs receive natal kicks comparable to those of single pulsars (e.g., Miller-Jones 2014; Mirabel 2017 and references therein). These astrometric observations have been used as constraints to theoretical models of BH X-ray binaries inferring that a natal kick is necessary for the formation of at least some low-mass BH X-ray binaries (e.g., Brandt et al. 1995; Willems et al. 2005; Fragos et al. 2009; Repetto et al. 2012; Mandel 2016; Repetto et al. 2017; Atri et al. 2019). On the other hand, studies focused on high-mass BH X-ray binaries, whose formation may be more closely related to double compact objects, provide no indications for natal kicks imparted onto the BHs (e.g., Wong et al. 2012, 2014; Valsecchi et al. 2010).

The description of compact-object formation and kicks depends on asymmetries developed during core collapse. 1D simulations cannot capture the development of such asymmetries, as this is an intrinsically 3D process. In addition, 3D simulations of core collapse provide evidence for the existence of the fallback BH formation scenario, at least for some BH progenitor stars (see Kuroda et al. 2018; Ott et al. 2018), and the natal kicks imparted on these BHs may also depend on the asymmetric distribution of fallback material (see Janka 2013, 2017). At the same time, however, 3D core-collapse simulations are very computationally expensive, and the explosion is rarely followed long enough in time to determine self-consistently the details of the fallback process, let alone perform a parameter study of different progenitors. Hence, despite the aforementioned caveats, high-resolution parameter studies using 1D core-collapse simulations are the only viable avenue to incorporate our current understanding of the core-collapse process into BPS studies.

In this work we explore the effects of the core-collapse mechanism on the formation of coalescing BHNSs, such as GW190426_152155, and their potential observability as electromagnetic transients. We consider a core-collapse prescription based on 1D core-collapse simulations and study the effect of nonmonotonic stellar explodability, with respect to the precollapse mass of the core. Finally, we discuss what we can learn in the future in terms of formation pathways, core-collapse physics, and NS equation of state, once observations put firmer constraints on the BHNS merger rate density and the fraction of them accompanied by an EMC.

2. Methods

We use the software framework POSYDON[7] to evolve populations of binaries for this study. POSYDON allows, among other functionalities, coupling of rapid BPS codes with grids of detailed binary evolution models for different phases of a binary's evolution. In this work, we coupled the rapid BPS code COSMIC (Breivik et al. 2020) to evolve binaries from the zero-age main sequence (ZAMS) until the first compact object strips its companion, and a grid of ~170,000 detailed binary evolution models ran with the MESA code (Paxton et al. 2011, 2013, 2015, 2018, 2019) to follow the final evolutionary

---

[7] https://posydon.org

phase of a BHNS progenitor, i.e., that of a binary consisting of a stripped He star and a compact object in a close orbit. This allows us to predict the spin of the second-born compact object (see Bavera et al. 2021, for a detailed description of the simulation setup).

For all populations evolved, we consider the following initial binary properties: the mass of the most massive star m_1 is distributed by the Kroupa (2001) initial mass function in a mass range of [5, 150] $M_\odot$. We assume that the mass ratio at birth is distributed uniformly as $q \in [0, 1]$ (Sana et al. 2012), setting a minimum mass for the secondary star at 0.08 $M_\odot$. The initial orbital periods are distributed in the range of [0.4, $10^{5.5}$] days as in Sana et al. (2012), extending the distribution for low values with a flat distribution as in Bavera et al. (2021). All binaries have zero birth eccentricity, and we assume an overall binary fraction $f_b = 0.7$ (see Sana et al. 2012; Bavera et al. 2021). For each model, we evolve 5×10^6 binaries per metallicity, for 10 different metallicity values, $Z \in [0.0001, 0.0002, 0.0003, 0.0006, 0.001, 0.0018, 0.0031, 0.0055, 0.0098, 0.0174]$. This corresponds to a total stellar mass of $\sim 5 \times 10^8$ $M_\odot$ for the underlying stellar population, per metallicity bin, and corresponds to a fraction of the initial mass function of $f_{corr} = 0.212$, i.e., the fraction of mass evolved by our initial conditions if the integral of the initial mass function over its entire range is normalized.

We use the same set of physical model parameters as in Bavera et al. (2021). Specifically, we infer the mass transfer (MT) stability according to a combination of critical mass ratio values, q_{crit}, for stars at different states. For MS donor stars $q_{crit} \simeq 1.72$, for Hertzsprung's gap stars $q_{crit} \simeq 3.83$, and for stars on the giant branch and the asymptotic giant branch we use fits from Hjellming & Webbink (1987), and for stripped stars we adopt q_{crit} as in Claeys et al. (2014). For stable MT, we assume that the accretion onto a compact object is Eddington limited, while the accretion onto a nondegenerate star is limited by the thermal timescale of the accretor (see Equations (64) and (65) in Hurley et al. 2002). Unstable MT is modeled with the classical $\alpha_{CE} - \lambda$ common-envelope (CE) formalism (van den Heuvel 1976; Webbink 1984), where we assume an $\alpha_{CE} = 1$ and λ_{CE} fits from Claeys et al. (2014) without taking into account the ionization energy of the envelope. Moreover, we assume the pessimistic CE scenario, namely, all systems that start CE evolution with a star in the Hertzsprung's gap are considered to merge owing to the unsuccessful envelope ejection (Ivanova & Taam 2004; Belczynski et al. 2007). The electron-capture SN (ECSN) prescription described in Podsiadlowski et al. (2004) is used, which maps helium-core masses in the range of [1.4, 2.5] $M_\odot$ to remnant baryonic mass 1.38 $M_\odot$ as in Giacobbo & Mapelli (2020). For the pair-instability and pulsational pair-instability SNe we consider the prescription by Marchant et al. (2019), which limits the maximum BH mass at $\sim 44\, M_\odot$.

To model the core collapse, in addition to the "rapid" and "delayed" mechanisms by Fryer et al. (2012), we implement a new prescription based on 1D core-collapse simulations. We use the publicly available data on pre-SN models and the remnant properties produced by the N20 engine of Sukhbold et al. (2016). We should stress here that our choice of the specific set 1D simulations does not imply that it is necessarily an improvement, in terms of physical realism, over the prescriptions by Fryer et al. (2012). However, the 1D core-collapse simulations by Sukhbold et al. (2016) based on the

Table 1
Definition of the Models Used to Evolve the Binary Stellar Populations

Model Name	σ_{ECSN} (km s^{-1})	σ_{FeCCSN} (km s^{-1})	NS Kicks	BH Kicks
STANDARD	20	265	Fallback weighted	Fallback weighted
FULL-ECSN -KICK	265	265	Fallback weighted	Fallback weighted
NO-BH -KICK	20	265	Fallback weighted	No kicks

N20 engine capture well a trend that appears in many recent studies of the nonmonotonic (in terms of initial mass) stellar explodability. It is this trend that we aim to study here.

Core-collapse prescriptions on BPS are maps from the stellar core properties to the compact-object mass and the fallback mass after the SN explosion. While the "rapid" and "delayed" prescriptions map the CO core mass at the pre-SN phase to the remnant's baryonic mass, $M_{rem,bar}$, for the implementation of the N20 engine we consider the He-core mass of the star at the pre-SN phase, $M_{He,core}$, to predict $M_{rem,bar}$, taking into account whether the SN explosion is predicted to be successful or not. The fallback mass for each SN is taken directly from Sukhbold et al. (2016), and SN kick magnitude is then estimated following the fallback-weighted kick prescription from Belczynski et al. (2008). As virtually all BHs produced by our implementation of N20 are considered to be produced by direct collapse, the fallback fraction in those cases is equal to 1, and therefore the kick velocity is zero. A complete description of the implementation of the engine in our BPS study is given in Appendix A.

For each mechanism three populations were produced with the assumptions described in Table 1. Our fiducial model, called STANDARD, considers a Maxwellian distribution with $\sigma_{ECSN} = 20$ km s^{-1} for kicks imparted on NSs formed from ECSNe and $\sigma_{FeCCSN} = 265$ km s^{-1} for Fe core-collapse SNe (FeCCSNe); the kicks in this model are fallback weighted as in Belczynski et al. (2008). The FULL-ECSN-KICK model considers that NSs formed from ECSNe and FeCCSNe receive the same kicks ($\sigma_{ECSN} = \sigma_{FeCCSN} = 265$ km s^{-1}). Finally, the NO-BH-KICK model considers that BHs receive no natal kicks, even if they are not produced by direct collapse.

While the evolution of binaries from ZAMS to the formation of a compact object plus an He star was computed with the rapid code COSMIC, the last phase of the evolution of a close compact object plus an He star was performed by interpolating a grid constituted by 172,570 detailed MESA binary evolution models. This last step allows us to derive more accurate estimates of the second-born compact object's spin (Qin et al. 2018; Bavera et al. 2020). The details on the grid and its interpolation are discussed in Appendix B.

We extract the BHNS mergers, systems that merge owing to gravitational wave radiation emission in less time than the current age of the universe (here taken as ~ 13.8 Gyr based on Planck Collaboration et al. 2016), and compute the number of BHNS mergers per unit mass. The merging timescale, by gravitational wave radiation, is computed according to Peters (1964). Adopting the ΛCDM cosmology, we distribute the BHNS across the metallicity-dependent cosmic star formation history, assuming that metallicities follow a truncated
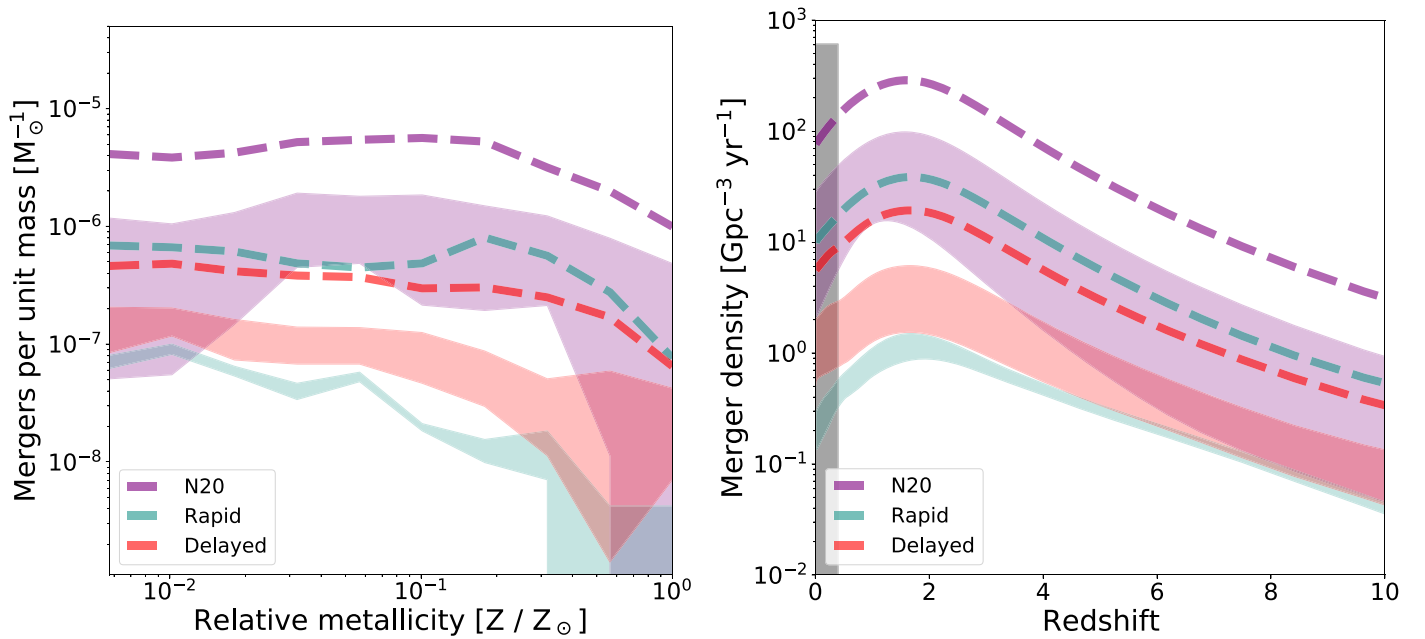
Figure 1. BHNS mergers per unit mass in terms of relative metallicity to the solar value (left) and its translation to the merger density rate history as a function of redshift z (right) for the STANDARD model. The dashed lines represent the whole population of BHNS mergers, while the contours enclose the number of EMCs by considering the three values of NS radius as described in Section 2, where upper and lower boundaries of the contours are the predictions taking into account $R_{\rm NS} = 13$ km and $R_{\rm NS} = 11$ km, respectively. In the right panel, the gray vertical bar is the 90% confidence interval of the local BHNS merger density rate reported in GWTC-1.

lognormal distribution with standard deviation 0.5 dex around the redshift-dependent empirical mean metallicity function derived by Madau & Fragos (2017). We compute the merger rate densities and detection rates as in Bavera et al. (2021), assuming the simulated "mid high/late low" LVC O3 detector sensitivity (Abbott et al. 2018), by considering a single detector signal-to-noise ratio threshold > 8 that simulates a two-network detector (see Barrett et al. 2018). Finally, we compute the fraction of events that produce EMCs. We assume that a BHNS merger will produce an EMC if the mass outside the BH ISCO after the merger, $M^{\rm ejecta}$, is greater than zero. The complete description on the computation of $M^{\rm ejecta}$ is described in Appendix C. Taking into account uncertainties in NS equation of state (e.g., Capano et al. 2020; Chatziioannou 2020, and references therein), we consider three different constant values for the NS radius, $R_{\rm NS} \in [11, 12, 13]$ km, to compute $M^{\rm ejecta}$ and, hence, predict the occurrence EMCs.

3. Results

3.1. The Theoretical Merger Rates of BHNS

The left panel of Figure 1 shows the number of BHNS mergers per unit mass, namely, the total evolved mass corrected by the initial mass function and the binary fraction, in terms of metallicity for the STANDARD model. In that panel the dashed lines represent the whole population of BHNSs for each core-collapse mechanism, while the shaded regions represent the subset of systems that will reproduce an EMC. The upper boundary of a shaded region is defined for $R_{\rm NS} = 13$ km, while the lower boundary is delimited by considering $R_{\rm NS} = 11$ km. By distributing the mergers on the cosmic star formation history, we find the merger density history in terms of redshift, shown in the right panel of Figure 1. There, we see that the local merger density for all core-collapse mechanisms is consistent with the upper limit reported on GWTC-1 (see Abbott et al. 2019) and plotted as the

gray shaded region. Furthermore, these results are consistent with other recent BPS studies (e.g., Giacobbo & Mapelli 2018; Neijssel et al. 2019; Drozda et al. 2020; Belczynski et al. 2020).

We show the detection rate of BHNSs for simulated O3 LIGO/Virgo sensitivity for all the populations in the top panels of Figure 2. The estimated BHNS detection rates are plotted with open diamonds, while the filled symbols represent the subset of systems that will produce an EMC for different values of $R_{\rm NS}$. All the rates shown in the top panels of Figure 2 are also summarized in Table 2. The most striking feature of Figure 2 is that detection rates from the N20 engine (the purple diamonds) are higher by a factor of ~ 2–10 with respect to the predictions for the "rapid" and "delayed" mechanisms in all models. This is because the N20 engine predicts the formation of low-mass BHs by direct collapse. These BHs do not receive natal kicks, which would otherwise disrupt the binary, and they are produced by less massive stars whose number is favored by the initial mass function.

To explore further the role of BH natal kicks on the detection rates of BHNS mergers, we focus on the NO-BH-KICK model (top right panel of Figure 2). The assumption of no BH kicks increases the detection rate for the "delayed" mechanism by a factor of ~ 4 with respect to the STANDARD model. In contrast, the rate for the "rapid" prescription does not have a significant increase between models. This difference is due to the fact that the pre-core-collapse He-core mass ($M_{\rm He,core}$) range, where the "rapid" mechanism predicts BH formation via partial fallback and nonzero kick velocities, is smaller ($M_{\rm He,core} \in [9, 13]M_{\odot}$) compared to the "delayed" mechanism ($M_{\rm He,core} \in [6, 13]M_{\odot}$), as shown in Figure 3. Furthermore, since this region is located at higher $M_{\rm He,core}$ values for the "rapid" mechanism, the steepness of the initial mass function results, in any case, in fewer BHs with nonzero kicks. Despite all of this, the N20 engine produces more than twice as many BHNS mergers, even when only considering the NO-BH-KICK models. This is explained by the fact that low-mass BHs
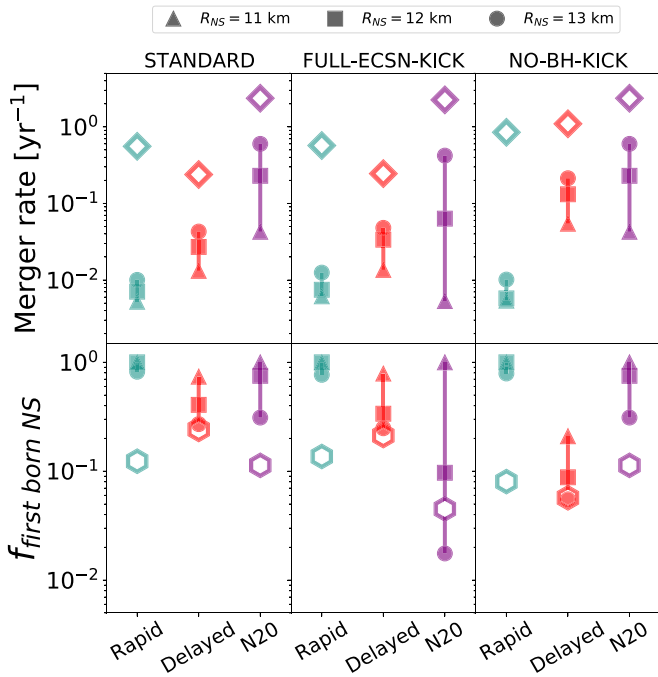
Figure 2. Predicted merger rate of BHNS populations for O3a (top panels) and the fraction of systems with first-born NSs $f_{\text{first born NS}}$ (bottom panels). These predicted rates are plotted each core-collapse mechanism and each model, respectively; see labels. In the top panels, the open diamonds indicate the predicted detection rate for the whole population of BHNSs, while the filled markers indicate the EMCs considering different NS radii; see legend above. In the bottom panels, the open hexagons denote the detected fraction of BHNSs with first-born NSs with respect to the whole population of detected mergers, while the filled markers are the fractions of EMCs from systems with first-born NSs with respect to all of them; see legend above for the shape description.

formed by the "delayed" mechanism in the NO-BH-KICK model are not produced by direct collapse, meaning that only a fraction (as low as ∼30%) of the pre-SN mass of their progenitors will collapse and the orbit of the binary needs to be readjusted, due to neutrino emission, even if the BH does not receive a natal kick. The readjustment of the orbit in such cases reduces the number of BHNS mergers with respect to the amount expected if the low-mass BHs were produced by direct collapse.

3.2. Rates of Electromagnetic Counterparts Linked to BHNS Mergers

The predicted rates of EMCs considering three different values for NS radii, 11, 12, and 13 km, are shown in the top panels of Figure 2 with the triangle, square, and circle markers, respectively. The predicted EMC rates for the N20 engine in the STANDARD population remain higher than the ones predicted using the other core-collapse prescriptions and for all NS radii. Note, however, that it is the "delayed" mechanism that has the largest fraction of BHNS mergers with EMCs. This can be understood from the fact that among the three mechanisms considered, it is only the "delayed" that can produce low-mass BHs, in the range of 2.5–3.5 $M_\odot$. These low-mass BHs, even when they are nonspinning, are able to disrupt a relatively compact ($\lesssim 12$ km) NS outside their ISCO.

For the "rapid" and N20 engines and assuming NS radii $\lesssim 12$ km, BHNS mergers with EMCs are only produced when the NS is the first-born compact object that subsequently tidally spins up the BH progenitor star and produces a highly

spinning BH. The bottom row of Figure 2 shows that although the fraction of first-born NSs in BHNS merges, for the "rapid" and N20 engines, is ∼10%, the fraction of BHNS mergers with EMCs that had a first-born NS is close to 100%.

The formation of the first compact object occurs in a wide orbit. Since the probability of the binary to remain bound after an SN kick scales with the ratio of the orbital velocity over the kick velocity (Kalogera 1996), an NS formed via FeCCSN, which typically receives a natal kick of hundreds of kilometers per second, will disrupt the binary. With the N20 engine, however, as BHs may be produced by $M_{\text{He,core}}$ as low as ∼ 4.5 $M_\odot$, a nonnegligible fraction of first-born NSs may come from progenitors with pre-core-collapse $M_{\text{He,core}}$ low enough to result in an ECSN. The low kicks associated with ECSNe increase significantly the survivability of these relatively rare binary configurations. We should note that theoretical models have shown that binary interactions can widen the core mass range that leads to ECSNe (see, e.g., Poelarends et al. 2017, and references therein). This may lead to an increased contribution of the pathway described above.

The FULL-ECSN-KICK models allow us to quantitatively explore the role of ECSNe on the formation of BHNSs with EMCs, which, as explained above, affects models with the N20 engine. Increasing the ECSN kick velocities has primarily an impact on the systems with first-born NSs rather than the whole population of BHNSs. From Table 2, we see that the BHNS merger detection rate slightly decreases for N20 from STANDARD to FULL-ECSN-KICK. Contrarily, such rates for the other core-collapse mechanisms remain similar, as the fraction of first-born NSs from ECSNe is negligible in those cases.[8] Most importantly, though, high ECSN kicks decrease the rate of BHNSs with EMCs in the N20 engine by a factor of ∼4, for NS with radii $\lesssim 12$ km; see Table 2.

Current constraints on the NS equation of state indicate that NS radii can be as high as 13 km (see Capano et al. 2020; Chatziioannou 2020, and references therein). This parameter has a crucial impact on the population of EMCs from BHNS mergers where the BH is the first-born compact object. In such cases the BH spin is negligible; therefore, an R_{NS} on the high end of the allowed parameter space is crucial to achieve an NS tidal disruption (Foucart et al. 2018). In fact, for $R_{\text{NS}} = 13$ km the maximum BH mass that can tidally disrupt an NS is below the minimum BH mass predicted by the N20 engine. This allows for BHNS mergers with EMCs originating from binaries with nonspinning, first-born BHs and translates to an increase by a factor of 15 and 2.5 of EMCs, compared to the assumed R_{NS} of 11 km and 12 km, respectively.

3.3. The Role of the SN Engine on the Synthesis of GW190426_152155-like Events

The estimation for the BHNS merger rate from the LVC O3a run, 2–4 yr^{-1}, is closer to the results from the N20 engine on all populations, as well as for the "delayed" one for the NO-BH-KICK population, favoring the engines that predict low-mass BHs with negligible SN kicks. We compute the merger rate of

---

[8] In fact, we do see a very small increase in the detection rate for those models, which is, however, above the Poisson error of our simulations. This very small increase may be explained by the fact that in those models some of the second-born NSs are produced by ECSNe. Imparting a larger natal kick on those NSs will not disrupt the binary, as its orbit is very close at that point in time, but will impart some eccentricity in the post-SN orbit, which may shorten the time to merge due to GW emission. This in turn can have a small effect on the overall rate.

Table 2
Predicted Local Detection Rates, $\mathcal{R}^{\mathrm{det}}$ (Detected Mergers per Year), for the LVC's Third Observing Run

Population	R_{NS}	STANDARD			FULL-ECSN-KICK			NO-BH-KICK		
		$\mathcal{R}^{\mathrm{det}}_{\mathrm{N20}}$	$\mathcal{R}^{\mathrm{det}}_{\mathrm{Rapid}}$	$\mathcal{R}^{\mathrm{det}}_{\mathrm{Delayed}}$	$\mathcal{R}^{\mathrm{det}}_{\mathrm{N20}}$	$\mathcal{R}^{\mathrm{det}}_{\mathrm{Rapid}}$	$\mathcal{R}^{\mathrm{det}}_{\mathrm{Delayed}}$	$\mathcal{R}^{\mathrm{det}}_{\mathrm{N20}}$	$\mathcal{R}^{\mathrm{det}}_{\mathrm{Rapid}}$	$\mathcal{R}^{\mathrm{det}}_{\mathrm{Delayed}}$
All		2.37	0.56	0.24	2.25	0.57	0.25	2.37	0.85	1.10
EMC	11 km	0.04	0.01	0.01	0.01	0.01	0.01	0.04	0.01	0.05
	12 km	0.23	0.01	0.03	0.06	0.01	0.03	0.23	0.01	0.13
	13 km	0.6	0.01	0.04	0.42	0.01	0.05	0.6	0.01	0.21
GW190426-like		0.56	0.03	0.06	0.55	0.05	0.07	0.56	0.12	0.42
GW190426 EMC	11 km	0.00	0.00	0.00	0.00	0.00	0.00	0.00	0.00	0.00
	12 km	0.01	0.00	0.00	0.00	0.00	0.00	0.01	0.00	0.00
	13 km	0.05	0.00	0.02	0.03	0.00	0.01	0.05	0.00	0.03

Note. Results here are for the whole population of BHNSs (All), for the EMCs, and for systems like GW190426_152155 (GW190426-like), as well as the subset of GW190425-like systems that will produce an EMC (GW190426 EMC) for each physical model.
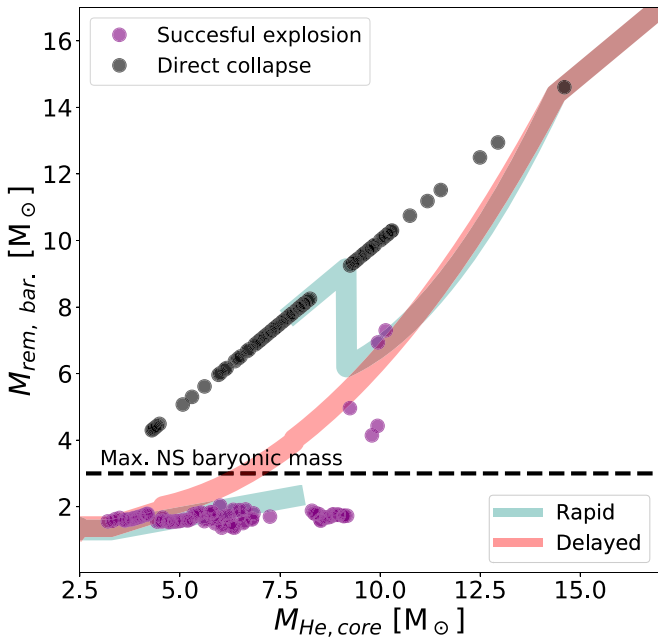

Figure 3. Baryonic remnant mass, $M_{\mathrm{rem,bar}}$, as a function of the He-core mass at the pre-SN phase, $M_{\mathrm{He,core}}$, from the N20 engine of Sukhbold et al. (2016) (circles), and for the "rapid" and "delayed" (red and turquoise thick lines) mechanisms from Fryer et al. (2012). For illustrative purposes we assume that the mass of the carbon–oxygen core is $0.76 M_{\mathrm{He,core}}$. Each model exploded with the N20 engine is labeled as a successful explosion or direct collapse (i.e., failed explosion), with purple and black colors, respectively. The black dashed line represents the maximum NS baryonic mass, in our model, which corresponds to a maximum NS gravitational mass of $2.5\,M_{\odot}$.

systems like GW190426_152155, the only observed system labeled as a BHNS merger (Abbott et al. 2020a), by considering the 90% confidence intervals of the event's measured total mass, chirp mass, and effective spin. Those results are shown in Table 2 as the population "GW190426-like." The detection of a system similar to GW190426_152155 is favored by the N20 engine in all populations and by the "delayed" mechanism in the NO-BH-KICK populations, while the "rapid" prescription predicts a rate of only 0.03–0.12 yr^{-1}, indicating that the detection of an event with GW190426_152155-like properties is rare in such case.

We also computed the rate of GW190426_152155-like systems that will produce an EMC (population "GW190426 EMC" in Table 2). In all cases the rates of EMCs linked to events like GW190426_152155 are less than 0.1 yr^{-1}, translating to a probability of 0%–25% of EMCs per observed system. This low rate agrees with the lack of an electromagnetic signal linked to the observed event.

3.4. Comparison to BBH Merger Density Rates

In order to compare our models with measurements with better constraints, we compute the local BBH and BHNS merger density rates as shown in Table 3 of Appendix C. The N20 STANDARD model, which increases the likelihood of events like GW190426_152155, overpredicts the measured BBH merger density, as reported by Abbott et al. (2020a), by ~5 times, compared to the other collapse mechanisms that overpredict the rate by < 2 times. Again, this is because the N20 engine assumes that BHs are born without kicks. Similarly, "rapid" and "delayed" NO-BH-KICK overpredict the local BBH rate by the same amount. When looking carefully at the BBH's progenitor evolutionary pathway, we find that it is the CE channel that produces the majority of these merging BBHs contributing to the observed local rate density.[9] If, indeed, BHs are born without a kick, then the models are overproducing the systems going through and surviving CE and therefore the population of BBHs, as we expect the mixture of all formation channels to contribute to the whole population, which is what recent studies suggest (e.g., Kruckow et al. 2016; Pavlovskii et al. 2017; Klencki et al. 2021).

4. Discussion and Conclusions

In this work, we present BPS models exploring the role of core-collapse prescriptions, including results of 1D core-collapse simulations and the associated natal kicks, on the observability of BHNS systems, events like GW190426_152155, and their EMCs. A rapid BPS code has been used to model isolated binary stars from ZAMS until the first-born compact object strips its companion star. From that stage, the evolution of the system until the formation of the second-born compact object was followed by detailed binary evolution models, allowing for more accurate estimates of the spin of the second-born compact object. The latter is critical in determining whether the NS will be tidally disrupted by the

---

[9] Note that here we neglected the parameter space leading to chemical homogeneous evolution. Models fully consistent with our STANDARD "delayed" assumptions show that the contribution of this channel to the BBH local merger rate density is comparable to the CE and SMT contribution (du Buisson et al. 2020; Zevin et al. 2021).

Table 3
Predicted Local Rate Density $\mathcal{R}$ (in Units of $\mathrm{Gpc}^{-1}\,\mathrm{yr}^{-1}$)

	Channel	STANDARD			FULL-ECSN-KICK			NO-BH-KICK		
		$\mathcal{R}_{N20}$	$\mathcal{R}_{Rapid}$	$\mathcal{R}_{Delayed}$	$\mathcal{R}_{N20}$	$\mathcal{R}_{Rapid}$	$\mathcal{R}_{Delayed}$	$\mathcal{R}_{N20}$	$\mathcal{R}_{Rapid}$	$\mathcal{R}_{Delayed}$
BBH	CE	162.78	81.13	39.13	162.06	81.64	38.55	162.78	129.41	167.31
	SMT	39.73	33.05	31.27	41.43	33.6	31.08	39.73	31.38	26.36
	CE + SMT	202.51	114.18	70.4	203.49	115.24	69.63	202.51	160.79	193.67
BHNS	CE	74.96	7.28	2.59	66.36	7.59	2.93	74.96	14.66	30.18
	SMT	2.28	2.86	3.06	2.99	3.12	2.88	2.28	1.88	2.49
	CE + SMT	77.24	10.14	5.65	69.35	10.71	5.81	77.24	16.54	32.67

Note. Results here are shown for the CE and SMT channels separately and combined for both the populations of BBHs and BHNSs for each model.

BH, as spinning BHs increase significantly the probability of EMCs produced by BHNS mergers.

We find that the N20 SN engine predicts BHNS merger rates higher by an order of magnitude compared to the "rapid" and "delayed" mechanisms. This is a consequence of the formation of low-mass BHs by direct collapse that are predicted by SN engines from 1D core-collapse simulations, such as N20. In addition, the N20 engine predicts higher rates of EMCs while being consistent with the lack of observations of such events to date.

Our models show that future, more stringent constraints on the NS equation of state will allow us to distinguish between formation subchannels of BHNSs. A mean NS radius closer to 11 km would indicate that the information from future observations of BHNS EMCs is linked to systems where the NS is the first-born compact object, as compact NSs are harder to disrupt by nonspinning BHs. In contrast, evidence of a larger radius (such as Riley et al. 2019; Abbott et al. 2020) will help us to infer information of low-mass BHs and possible natal kicks linked to their formation.

Finally, we find that the synthesis of events like GW190426_152155 is favored by SN engines that produce low-mass BHs with small or no SN kicks. The N20 engine predicts a rate of $\sim 0.6\,\mathrm{yr}^{-1}$ for such an event, one order of magnitude higher than the predictions by the "rapid" and "delayed" mechanisms in the STANDARD model, and 30% larger than the result from "delayed" with the NO-BH-KICK model. However, such mechanisms overestimate the BBH local merger density rate, with most of the predicted merging BBHs going through the CE evolution channel. Detailed binary evolution calculations suggest that the source of this apparent discrepancy may be the parameterizations of MT stability criteria and envelope binding energy estimates, which, as implemented in most BPS codes may, severely overpredict the number of BBH progenitor systems going through and surviving the CE phase. In any case, our results highlight that the predictions on local merger density rates of BHNSs and BBHs are highly sensitive to the uncertainties on the kick velocity prescription. While core-collapse physics remains uncertain, our results show the importance of considering the uncertainties linked to the current physical prescriptions and the impact on the synthesis of compact binary mergers.

Appendix A
Implementation of the N20 Engine

We consider the stellar models by Sukhbold et al. (2016), evolved in solar metallicity, to describe the baryonic mass of the final remnant. Binary interactions can affect the compactness of the pre-SN core (see Schneider et al. 2021) compared to expectations from single stars, but the general nonmonotonic trend of stellar explodability is preserved for binaries, as well as for different metallicities (O'Connor & Ott 2011; Patton & Sukhbold 2020). We apply the prescription deduced from the results of Sukhbold et al. (2016) to stars in binary systems and in a range of metallicities, as we aim to explore the effect of the average nonmonotonic explodability trends rather than predicting accurately the compactness of the core.

Figure 3 shows the baryonic remnant mass as a function of $M_{\mathrm{He,core}}$, for the N20 engine (Sukhbold et al. 2016), with the "rapid" and "delayed" mechanisms (Fryer et al. 2012). In the same figure, each stellar model, collapsed with N20, is classified as a successful explosion or a direct collapse depending on whether the SN shock is revived by the neutrino flux or not, respectively. In the case of the N20 engine, to predict whether a star will undergo a successful explosion or direct collapse, we extract the result in terms of the nearest neighbor of the star's $M_{\mathrm{He,core}}$ with respect to the results from Sukhbold et al. (2016). If the star is classified as a progenitor of a successful explosion, its $M_{\mathrm{rem,bar}}$ will have the same value of the remnant baryonic mass associated with the point with the nearest value for $M_{\mathrm{He,core}}$. Otherwise, if the star is classified as a progenitor of a direct collapse, then $M_{\mathrm{rem,bar}}$ is equal to the pre-SN mass of the star.

To determine whether the remnant is a BH or an NS, we calculate the remnant gravitational mass considering the neutrino loss as in Zevin et al. (2020), where the maximum mass loss by neutrinos is considered to be $0.5\,M_\odot$ (corresponding to 9×10^{53} erg). If the remnant gravitational mass is larger than $2.5\,M_\odot$, we assume that the compact object is a BH; otherwise, we assume that it is an NS. For this work, the successful explosions that produce massive remnants that will end up as BHs were not considered, as such cases are rare (from Sukhbold et al. 2016, only 5 models from 105 successful explosions form a BH for the N20 engine). Motivated by multidimensional 3D core-collapse studies, semianalytical core-collapse models have been proposed in the literature (e.g., Couch et al. 2020; Mandel & Müller 2020), where the production of BHs by successful explosions is not as rare as in 1D simulations. But the trend of nonmonotonic explodability is also preserved between the semianalytical prescriptions and 1D core-collapse simulations. As the production of successful explosions and their final remnants is still uncertain, we consider that the results from Sukhbold et al. (2016) are compatible with the expectations and trends described with the latest semianalytical core-collapse prescriptions.

Appendix B
Grids of Detailed NS/BH–He-star Models

We use a subset of detailed MESA models (Paxton et al. 2011, 2013, 2015, 2018, 2019) of BH–He-star systems of Bavera et al. (2021), which we extend to cover the NS star and low He-star masses. These models treat the compact object as a point mass; hence, they can be applied to simulate NS–He-star systems. For simplicity, we assumed that all physical assumptions made in the BH–He-star regime apply also to the NS–He-star regime, including an Eddington mass accretion rate limit of $\dot{M}_{\rm Edd} = 7.36 \times 10^{-8}(M_{\rm BH/NS}/M_\odot)M_\odot\,{\rm yr}^{-1}$. The selected subset of the original grid covers the initial parameter space of 10 metallicities, Z, in the log-range [0.0001, 0.0174] in log-steps of $\Delta \log_{10}(Z) \simeq 0.25$, 11 BH masses in the log-range [2.5, 54.4] $M_\odot$, 17 He-star masses in the log-range [8, 80] $M_\odot$, and 20 binary periods in the log-range [0.09, 8] days. We extend this data set to cover 10 NS masses in the log-range [1, 2.28] $M_\odot$; 26 He-star masses where 20 are in the log-range [3, 12] $M_\odot$, 5 in the range [3, 7] $M_\odot$ (only for BH masses), and 1 at $2.5\,M_\odot$; and an extra period at 0.04 days. The smallest He-star mass is chosen to guarantee coverage of the parameter space down to white dwarf formation, while the maximum He-star mass and smallest orbital period were chosen to include the full range of compact-object–He-star systems produced by our COSMIC models. The wide orbital period range ensures that we cover the parameter space well past the point where any BHNS or BBH system will merge within the age of the universe. The original grid subset consisting of 37,400 models was therefore extended to a total of 172,740 MESA models. The fraction of failed MESA runs varies from 0.6% to 1.5% depending on metallicity. In Figure 4 we show two 2D slices of the 4D parameter space sliced at $Z = 0.00312$ and $m_{\rm NS} = 1.44\,M_\odot$ and $m_{\rm BH} = 8.57\,M_\odot$, respectively, where we indicate with a color the final He-star mass and angular momentum given the initial orbital separation and He-star masses of the detailed simulations.

We should note that in constructing the grid described above, we have made the assumption that both CE and stable MT strip completely the hydrogen-rich envelope. This is, in

fact, a simplifying assumption made by all rapid BPS codes, including COSMIC. Detailed stellar structure models and 1D hydrodynamical simulations of CE (e.g., Fragos et al. 2019; Marchant et al. 2021) and stable envelope stripping (e.g., Sravan et al. 2019; Laplace et al. 2020) in binary systems have shown that some hydrogen might remain on the envelope of stripped stars, especially at low metallicity, which might lead to re-expansion and a new binary interaction phase (Laplace et al. 2020). Our models do not capture those effects.

These grids were used to determine the final outcomes and final parameters of the late-end evolution stage of the binary systems through linear interpolation. Each metallicity is interpolated separately. We want to interpolate five quantities A_i: the He-star mass, angular momentum and its carbon–oxygen core mass, orbital period before the SN, and the lifetime of the binary. Before interpolating each quantity, we log-transformed it and rescale it to the interval $[-1, 1]$ to assign equal weight to each dimension during the interpolation. The interpolation[11] itself relies on building a Delaunay triangulation of the input data points followed by barycentric linear interpolation over the vertices of the (hyper)triangle containing the location of interest. We test the accuracy of the interpolation computing relative errors of a test grid that is composed of an arbitrary fraction (5%) of runs that we excluded from the train sample. To obtain a consistent estimate, we repeat this experiment 10 times for each metallicity and each interpolated quantity. If a point of a nonphysical region of the parameter space (e.g., zero-age He main sequence [ZAHeMS] overflow, max MT or L2 overflow) is correctly interpolated to NaN (not a number) by the algorithm, we consider it to have a zero relative error. On the other hand, if a point is wrongly interpolated to NaN, we consider it to have a relative error of 1. In Figure 5 we report the median relative error of each transformed and rescaled quantity $X_i \equiv \log_{10}(A_i)^{[-1,1]}$ as $\Delta_i = |X_{\rm true,i} - X_{\rm interp,i}|/X_{\rm true,i}$. Because of the large sample of data points, we find small interpolation errors. Most of the quantities show an increase of median relative error as a function of metallicity. This is caused by the fact that at high metallicity the grids show a less linear behavior than at low metallicity. This nonlinearity is a direct consequence of He-star stellar winds, which, in our models, scale as $(Z/Z_\odot)^{0.85}$. In these systems, the He stars lose a nonnegligible amount of mass and the orbits widen considerably. Moreover, NS–He-star systems in tight orbits have a higher probability to initiate an MT case owing to the He-star tendency to expand more than at low metallicity.

Appendix C
BHNS Electromagnetic Counterpart Condition

We consider the model of Foucart et al. (2018) to determine the mass of the NS that remains outside the BH ISCO after the tidal disruption, as

$$\left[\max\left(\alpha \frac{1 - 2C_{\rm NS}}{\eta^{1/3}} - \beta \hat{R}_{\rm ISCO} \frac{C_{\rm NS}}{\eta} + \gamma, 0\right)\right]^\delta M_{\rm NS}, \quad (C1)$$

where $\alpha = 0.406$, $\beta = 0.139$, $\gamma = 0.255$, $\delta = 1.761$, $\hat{R}_{\rm ISCO} \equiv \frac{R_{\rm ISCO}c^2}{GM_{\rm BH}}$, $C_{\rm NS} = Q\frac{\hat{R}_{\rm ISCO}}{\hat{R}_{\rm ISCO}R_{\rm NS}}$, $Q = \frac{M_{\rm BH}}{M_{\rm NS}}$, and

---

[11] We used the LinearNDInterpolator function of the scipy (Virtanen et al. 2020) Python library, which is based on the Quickhull algorithm (Barber et al. 1996).
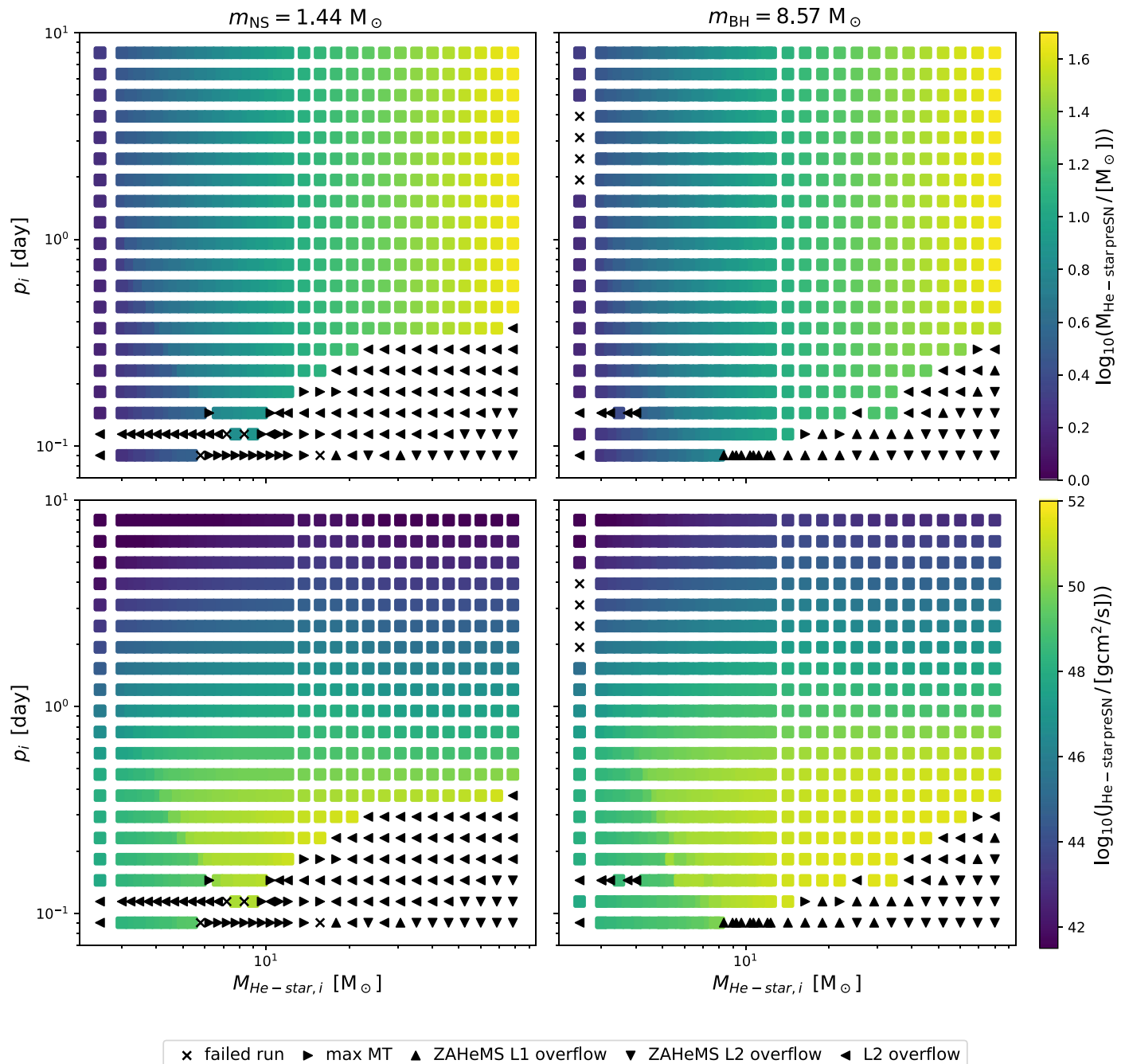
Figure 4. Two 2D slices of the 4D MESA grid for $Z = 0.00312$ and $m_{NS} = 1.44\ M_\odot$ and $m_{BH} = 8.57\ M_\odot$, respectively. The final He-star mass and angular momentum pre-SN values are colored for each successful track according to each color bar. Each successful run stopped because of carbon depletion or off-center neon ignition (square markers), while other termination flags are shown in the bottom legend. For visualization purposes, the models at $p = 0.04$ days were excluded from the figure as those runs resulted in ZAHeMS L1 or L2 Roche lobe overflow.

$\eta = Q/(1 + Q)^2$. Here M_{BH} is the mass of the BH, M_{NS} is the mass of the NS, and R_{NS} is the radius of the NS. In this work we explore three values for R_{NS}: 11, 12, and 13 km.

Appendix D
BBH and BHNS Merger Rate Densities

To better understand the implication of the physical modeling assumptions done in this study, we also calculate the BBH merger rate densities. The latter are much better constrained by GWTC-2, which finds the local merger rate density of BBH to be $23.9^{+14.9}_{-8.6}$ Gpc^{-3}yr^{-1} (Abbott et al.

2020c). The BBH rate densities rising from the CE and stable MT (SMT) channels given the same set of assumptions made here (STANDARD-Delayed) are presented in Bavera et al. (2021). For a one-to-one comparison with BHNS rate densities of the different core-collapse and kick prescriptions considered in this work, we summarize the rate densities of BBHs and BHNS for the CE and SMT channels, as well as their combination, in Table 3.

In contrast to the original study done by Bavera et al. (2021), the new models differ in the following ways. First, we (i) simulated a metallicity range with one-third the resolution of Bavera et al. (2021) but verified that this does not have a
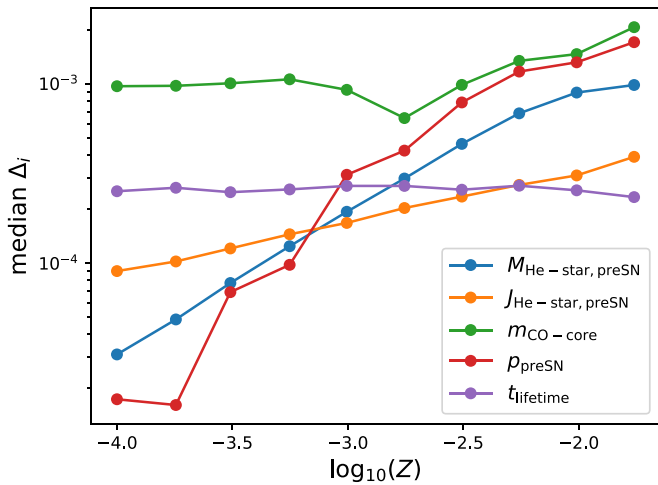
Figure 5. Median relative error as a function of metallicity of the log-transformed and rescaled five quantities A_i: the He-star mass (blue), angular momentum (orange) and its carbon–oxygen core mass (green) before the SN, the orbital period before the SN (red), and the lifetime of the binary (green).

noticeable impact on the rate estimates by reanalyzing Bavera et al. (2021) models with the same metallicity sample resolution. Second, (ii) the core-collapse of the secondary is assumed to be direct, whereas in the original study we followed the core collapse of the MESA He-star profile at SNe accounting for disk formation. When an accretion disk is formed, only a fraction of its mass falls to the hole (see Appendix D in Bavera et al. 2021), which, in practice, means that here tidally spun-up highly spinning BHs are slightly more massive compared to Bavera et al. (2021). Moreover, we only (iii) interpolate binary properties before the SN, while in the original work, which only investigated the delayed collapse mechanism, we also interpolated the second-born compact-object mass and spin (the former has, on average, a larger interpolation error compared to the pre-SN mass; see Figure E.1 of Bavera et al. 2021). Finally, we also updated the condition that determines BH formation. We assume that (iv) a BH is formed if the compact-object gravitational mass is larger than the maximum NS mass ($2.5\,M_\odot$), while in the previous work we assumed that a collapsing star leading to the formation of a BH had to have at least a carbon–oxygen core mass and a remnant baryonic mass of $3\,M_\odot$ in order to form a BH (as $0.5\,M_\odot$ were assumed to be lost because of neutrinos during the collapse of the proto-NS). We verified that this change has no impact on the results.

In Table 3 we can see that the STANDARD-delayed model predicts comparable rate densities of ~ 39 and $\sim 31\,\mathrm{Gpc}^{-3}\,\mathrm{yr}^{-1}$ for CE and SMT channels, respectively. These values are in agreement with Bavera et al. (2021), where the small deviation in the numbers is given by the changes explained in the previous paragraph. On the other hand, STANDARD-N20 overpredicts the CE+SMT rates compared to the observations by a factor of at least 5. This is because in the N20 engine all BHs are formed thorough direct collapse, without a kick. When assuming no natal kicks (other than the readjustment of the orbits because of neutrino mass loss), the NO-BH-KICK models with rapid and delayed predict similar rates to the N20 engine, meaning that the discrepancy is a direct product of no BH kicks. In fact, if nature were to agree with the N20 engine, then the formation of merging BBHs through the CE+SMT would overpredict the systems surviving these channels. When looking more carefully at the rate densities

of these models, we see that it is the CE channel that overpredicts the constraints from merging BBHs in the local universe. As recent studies have shown, the classical $\alpha_{\mathrm{CE}} - \lambda$ parameterization of CE and MT stability parameterization (q_{crit}) might overpredict the number of systems going through and surviving this evolutionary phase (e.g., Pavlovskii & Ivanova 2015; Kruckow et al. 2016; Pavlovskii et al. 2017; Klencki et al. 2021).

ORCID iDs

Jaime Román-Garza (ID) https://orcid.org/0000-0002-5962-4796
Simone S. Bavera (ID) https://orcid.org/0000-0002-3439-0321
Tassos Fragos (ID) https://orcid.org/0000-0003-1474-1523
Emmanouil Zapartas (ID) https://orcid.org/0000-0002-7464-498X
Devina Misra (ID) https://orcid.org/0000-0003-4260-960X
Jeff Andrews (ID) https://orcid.org/0000-0001-5261-3923
Scotty Coughlin (ID) https://orcid.org/0000-0002-0403-4211
Aaron Dotter (ID) https://orcid.org/0000-0002-4442-5700
Konstantinos Kovlakas (ID) https://orcid.org/0000-0003-3684-964X
Ying Qin (ID) https://orcid.org/0000-0002-2956-8367
Kyle A. Rocha (ID) https://orcid.org/0000-0003-4474-6528

References

Abbott, B., Abbott, R., Abbott, T., et al. 2020, ApJL, 892, L3
Abbott, B. P., Abbott, R., Abbott, T., et al. 2018, LRR, 21, 3
Abbott, B. P., Abbott, R., Abbott, T. D., et al. 2017a, ApJL, 848, L12
Abbott, B. P., Abbott, R., Abbott, T. D., et al. 2017b, ApJL, 848, L13
Abbott, B. P., Abbott, R., Abbott, T. D., et al. 2019, PhRvX, 9, 031040
Abbott, R., Abbott, T. D., Abraham, S., et al. 2020a, arXiv:2010.14527
Abbott, R., Abbott, T. D., Abraham, S., et al. 2020b, ApJL, 896, L44
Abbott, R., Abbott, T. D., Abraham, S., et al. 2020c, arXiv:2010.14533
Arca Sedda, M. 2020, CmPhy, 3, 43
Atri, P., Miller-Jones, J. C. A., Bahramian, A., et al. 2019, MNRAS, 489, 3116
Barber, C. B., Dobkin, D. P., & Huhdanpaa, H. 1996, ACM Trans. Math. Software, 22, 469
Barrett, J. W., Gaebel, S. M., Neijssel, C. J., et al. 2018, MNRAS, 477, 4685
Bavera, S. S., Fragos, T., Qin, Y., et al. 2020, A&A, 635, A97
Bavera, S. S., Fragos, T., Zevin, M., et al. 2021, A&A, 647, A153
Belczynski, K., Kalogera, V., Rasio, F. A., et al. 2008, ApJS, 174, 223
Belczynski, K., Klencki, J., Fields, C. E., et al. 2020, A&A, 636, A104
Belczynski, K., & Taam, R. E. 2008, ApJ, 685, 400
Belczynski, K., Taam, R. E., Kalogera, V., Rasio, F. A., & Bulik, T. 2007, ApJ, 662, 504
Brandt, W. N., Podsiadlowski, P., & Sigurdsson, S. 1995, MNRAS, 277, L35
Breivik, K., Coughlin, S. C., Zevin, M., et al. 2020, ApJ, 898, 71
Capano, C. D., Tews, I., Brown, S. M., et al. 2020, NatAs, 4, 625
Chatziioannou, K. 2020, GReGr, 52, 109
Claeys, J. S. W., Pols, O. R., Izzard, R. G., Vink, J., & Verbunt, F. W. M. 2014, A&A, 563, A83
Couch, S. M., Warren, M. L., & O'Connor, E. P. 2020, ApJ, 890, 127
Drozda, P., Belczynski, K., O'Shaughnessy, R., Bulik, T., & Fryer, C. 2020, arXiv:2009.06655
du Buisson, L., Marchant, P., Podsiadlowski, P., et al. 2020, MNRAS, 499, 5941
Ertl, T., Woosley, S. E., Sukhbold, T., & Janka, H.-T. 2020, ApJ, 890, 51
Foucart, F., Hinderer, T., & Nissanke, S. 2018, PhRvD, 98, 081501
Fragos, T., Andrews, J. J., Ramirez-Ruiz, E., et al. 2019, ApJL, 883, L45
Fragos, T., & McClintock, J. E. 2015, ApJ, 800, 17
Fragos, T., Willems, B., Kalogera, V., et al. 2009, ApJ, 697, 1057
Fryer, C. L., Belczynski, K., Wiktorowicz, G., et al. 2012, ApJ, 749, 91
Fuller, J., Piro, A. L., & Jermyn, A. S. 2019, MNRAS, 485, 3661
Giacobbo, N., & Mapelli, M. 2018, MNRAS, 480, 2011
Giacobbo, N., & Mapelli, M. 2020, ApJ, 891, 141
Han, M.-Z., Tang, S.-P., Hu, Y.-M., et al. 2020, ApJL, 891, L5
Herant, M., Benz, W., Hix, W. R., Fryer, C. L., & Colgate, S. A. 1994, ApJ, 435, 339

Hjellming, M. S., & Webbink, R. F. 1987, ApJ, 318, 794
Hobbs, G., Lorimer, D., Lyne, A., & Kramer, M. 2005, MNRAS, 360, 974
Hunter, J. D. 2007, CSE, 9, 90
Hurley, J. R., Tout, C. A., & Pols, O. R. 2002, MNRAS, 329, 897
Ivanova, N., & Taam, R. E. 2004, ApJ, 601, 1058
Janka, H.-T. 2013, MNRAS, 434, 1355
Janka, H.-T. 2017, ApJ, 837, 84
Kalogera, V. 1996, ApJ, 471, 352
Klencki, J., Nelemans, G., Istrate, A. G., & Chruslinska, M. 2021, A&A, 645, A54
Kroupa, P. 2001, MNRAS, 322, 231
Kruckow, M. U., Tauris, T. M., Langer, N., et al. 2016, A&A, 596, A58
Kuroda, T., Kotake, K., Takiwaki, T., & Thielemann, F.-K. 2018, MNRAS: Letters, 477, L80
Laplace, E., Götberg, Y., de Mink, S. E., Justham, S., & Farmer, R. 2020, A&A, 637, A6
Madau, P., & Fragos, T. 2017, ApJ, 840, 39
Mandel, I. 2016, MNRAS, 456, 578
Mandel, I., & Müller, B. 2020, MNRAS, 499, 3214
Marchant, P., Pappas, K. M. W., Gallegos-Garcia, M., et al. 2021, arXiv:2103.09243
Marchant, P., Renzo, M., Farmer, R., et al. 2019, ApJ, 882, 36
Miller-Jones, J. C. A. 2014, PASA, 31, e016
Mirabel, F. 2017, NewAR, 78, 1
Neijssel, C. J., Vigna-Gómez, A., Stevenson, S., et al. 2019, MNRAS, 490, 3740
O'Connor, E., & Ott, C. D. 2011, ApJ, 730, 70
Ott, C. D., Roberts, L. F., da Silva Schneider, A., et al. 2018, ApJL, 855, L3
Patton, R. A., & Sukhbold, T. 2020, MNRAS, 499, 2803
Pavlovskii, K., & Ivanova, N. 2015, MNRAS, 449, 4415
Pavlovskii, K., Ivanova, N., Belczynski, K., & Van, K. X. 2017, MNRAS, 465, 2092
Paxton, B., Bildsten, L., Dotter, A., et al. 2011, ApJS, 192, 3
Paxton, B., Cantiello, M., Arras, P., et al. 2013, ApJS, 208, 4
Paxton, B., Marchant, P., Schwab, J., et al. 2015, ApJS, 220, 15
Paxton, B., Schwab, J., Bauer, E. B., et al. 2018, ApJS, 234, 34
Paxton, B., Smolec, R., Schwab, J., et al. 2019, ApJS, 243, 10
Pejcha, O., & Thompson, T. A. 2015, ApJ, 801, 90
Peters, P. C. 1964, PhRv, 136, B1224

Planck Collaboration, Ade, P. A. R., Aghanim, N., et al. 2016, A&A, 594, A13
Podsiadlowski, P., Langer, N., Poelarends, A., et al. 2004, ApJ, 612, 1044
Poelarends, A. J. T., Wurtz, S., Tarka, J., Cole Adams, L., & Hills, S. T. 2017, ApJ, 850, 197
Pols, O. 1994, A&A, 290, 119
Price-Whelan, A. M., Sipőcz, B., Günther, H., et al. 2018, AJ, 156, 123
Qin, Y., Fragos, T., Meynet, G., et al. 2018, A&A, 616, A28
Rastello, S., Mapelli, M., Di Carlo, U. N., et al. 2020, MNRAS, 497, 1563
Repetto, S., Davies, M. B., & Sigurdsson, S. 2012, MNRAS, 425, 2799
Repetto, S., Igoshev, A. P., & Nelemans, G. 2017, MNRAS, 467, 298
Riley, T. E., Watts, A. L., Bogdanov, S., et al. 2019, ApJL, 887, L21
Robitaille, T. P., Tollerud, E. J., Greenfield, P., et al. 2013, A&A, 558, A33
Sana, H., De Mink, S., de Koter, A., et al. 2012, Sci, 337, 444
Schneider, F., Podsiadlowski, P., & Müller, B. 2021, A&A, 645, A5
Sipior, M. S., & Sigurdsson, S. 2002, ApJ, 572, 962
Spruit, H. 2002, A&A, 381, 923
Sravan, N., Marchant, P., & Kalogera, V. 2019, ApJ, 885, 130
Sukhbold, T., Ertl, T., Woosley, S., Brown, J. M., & Janka, H.-T. 2016, ApJ, 821, 38
Sukhbold, T., & Woosley, S. 2014, ApJ, 783, 10
Sukhbold, T., Woosley, S. E., & Heger, A. 2018, ApJ, 860, 93
Ugliano, M., Janka, H., Arcones, A., & Marek, A. 2012, in ASP Conf. Ser. 453, Advances in Computational Astrophysics: Methods, Tools, and Outcome, ed. R. Capuzzo-Dolcetta, M. Limongi, & A. Tornambè (San Francisco, CA: ASP), 91
Valsecchi, F., Glebbeek, E., Farr, W. M., et al. 2010, Natur, 468, 77
Van den Heuvel, E., & Yoon, S.-C. 2007, Ap&SS, 311, 177
van den Heuvel, E. P. J. 1976, in IAU Symp. 73, Structure and Evolution of Close Binary Systems, ed. P. Eggleton, S. Mitton, & J. Whelan (Cambridge: Cambridge Univ. Press), 35
Virtanen, P., Gommers, R., Oliphant, T. E., et al. 2020, Nature Methods, 17, 261
Webbink, R. F. 1984, ApJ, 277, 355
Willems, B., Henninger, M., Levin, T., et al. 2005, ApJ, 625, 324
Wong, T.-W., Valsecchi, F., Ansari, A., et al. 2014, ApJ, 790, 119
Wong, T.-W., Valsecchi, F., Fragos, T., & Kalogera, V. 2012, ApJ, 747, 111
Zevin, M., Bavera, S. S., Berry, C. P., et al. 2021, ApJ, 910, 152
Zevin, M., Spera, M., Berry, C. P., & Kalogera, V. 2020, ApJL, 899, L1